SAND2017-12933R

Sandia National Laboratories
Operated for the U.S. Department of Energy by
National Technology and Engineering Solutions of Sandia, Inc.
Albuquerque, New Mexico 87185

date: November 16, 2017

to: Distribution

from: Brian Lester (1554)

subject: Verification of the Skorohod-Olevsky Viscous Sintering (SOVS) Model

1 Introduction

Sintering refers to a manufacturing process through which mechanically pressed bodies of ceramic (and sometimes metal) powders are heated to drive densification thereby removing the inherit porosity of green bodies [1]. As the body densifies through the sintering process, the ensuing material flow leads to macroscopic deformations of the specimen and as such the final configuration differs from the initial. Therefore, as with any manufacturing step, there is substantial interest in understanding and being able to model the sintering process to predict deformation and residual stress. Efforts in this regard have been pursued for face seals [2], gear wheels [3], and consumer products like wash-basins [4].

To understand the sintering process, a variety of modeling approaches have been pursued at different scales [5]. At the mesoscale, kinetic Monte Carlo (KMC) simulations have been of interest both to study the kinetics of densification and impact of microstructural features as well as calibrate higher scale models [6, 7, 8]. At the continuum (macro-)scale of interest for production of parts like those listed above, a variety of three-dimensional constitutive models (*e.g.* [9, 10, 2, 11, 12]) have been postulated. In general, the formulations are motivated by the specifics and kinetics of different sintering types (*i.e.* solid-state [2], liquid [9], or viscous [10, 11]) and modeling terms and functions are constructed by assumptions regarding specific mechanisms.

One particular formulation of interest has been the Skorohod-Olevsky viscous sintering (SOVS) model popularized by Olevsky [10]. This model has been used (and extended) to model the manufacturing process of different systems (*e.g.* [12, 13, 4]). This constitutive representation includes a viscous, non-linear formulation. Thus, analyzing continuum level problems through the finite element method requires appropriate integration schemes for the local constitutive behavior and sufficient spatial and temporal discretizations of the global problem to resolve desired features. Constitutive implementations based on a semi-implicit formulation of McHugh and Riedel [9] have been used by many analysts [12] while others have leveraged features of commercial software [13]. Both the accuracy and robustness of the constitutive integration scheme as well as the complexity of the finite element problem can dictate required discretizations. In some efforts, difficulties in appropriately resolving temporal and spatial fields have been noted. For instance, as part of their efforts verifying and validating the SOVS model, Argüello *et al.* [12] (Section III.(2)) note,

> "However, it was found that the details of the deformation could not be adequately captured without a fairly fine mesh... From this it can be inferred that the curvature (and presumably warpage, etc.) cannot be captured in this model without significant mesh refinement. Therefore problems in which the accurate predictions of the details of the deformation of the part are sought will be computational intensive, requiring either long run-times or perhaps requiring the use of massively parallel computing."

Such an observation regarding the difficulty of using the SOVS (or other) sintering models can hinder the adoption and utilization of corresponding models. However, it is important to note that the investigation of Argüello *et al.* [12] used both a legacy finite element code (JAS3D) and the legacy constitutive implementation scheme of McHugh and Riedel [9]. Here, the possibility of mitigating these issues have been addressed by (*i*) proposing and implementing a new, fully implicit integration scheme, and (*ii*) investigating the possibility that such techniques can aid in both the spatial and temporal convergence characteristics of the global finite element problem. Section 2 briefly presents the SOVS sintering model and both legacy (McHugh-Riedel) and new (implicit) numerical implementation. Section 3 uses these implementations to revisit both constitutive verification (Section 3.1) and the bilayer bar verification (Section 3.2) problems of Argüello *et al.* [12]. Some conclusions and recommendations towards future research are given in Section 4.

2 Model

Before proceeding to the verification exercises, the SOVS model used in these studies is presented here for completeness. The specific theoretical form is given in Section 2.1 while both the existing McHugh-Riedel and new implicit integration scheme are discussed in Section 2.2.

2.1 Theoretical Model

The Skorohod-Olevsky viscous sintering (SOVS) model is a continuum mechanics based model for the 3D evolution of a powder-based material [10] undergoing the sintering process (see [2, 11, 12] for examples of utilization). In the case of the linear viscosity assumption, the inelastic (sintering) strain rate, $\dot{\varepsilon}^{\mathrm{in}}_{ij}$, may be written as,

$$\dot{\varepsilon}_{ij}^{\mathrm{in}} = \frac{\sigma'_{ij}}{2\eta_0(\theta)\,\phi(\rho)} + \frac{\sigma_{kk} - 3\sigma_s(\rho)}{18\eta_0(\theta)\,\psi(\rho)}\delta_{ij}, \tag{1}$$

in which σ_{ij}, σ'_{ij}, and $(1/3)\,\sigma_{kk}$ are the Cauchy stress, deviatoric stress, and pressure that are related via $\sigma_{ij} = \sigma'_{ij} + (1/3)\,\sigma_{kk}\delta_{ij}$ while η_0, ϕ, and ψ are the shear viscosity of the fully dense skeleton phase, normalized shear viscosity, and normalized bulk viscosity[1] and σ_s is the sintering stress. In addition to the Cauchy stress, the material state is also described by the temperature, θ, and relative density, $\rho = \rho_t/\rho_T$, where ρ_t is the density at time "t" and ρ_T is the theoretical density.

The general dependencies assumed here for the viscosities and sintering stress are denoted in Eqn. 1. Other research efforts have expanded the dependencies of these functions and various functional representations for each of the different terms have been proposed by modelers to capture different characteristics (see [2, 11, 12] for some examples). Here, the emphasis is on numerical performance and behavior the forms selected, studied, and verified by Arüello *et al.* [12] are used. These forms are given by,

$$\begin{aligned}
\phi(\rho) &= a_1\rho^{b_1}, \qquad \psi(\rho) = a_2\frac{\rho^{b_2}}{(1-\rho)^{c_2}}, && (2)\\
\sigma_s(\rho) &= \sigma_{s0}\bar{\sigma}_s(\rho), \qquad \bar{\sigma}_s(\rho) = a_3\rho^{b_3}, && (3)\\
\eta_0(\theta) &= a_4\left(\frac{\theta}{\theta_0}\right)^2 + b_4\left(\frac{\theta}{\theta_0}\right) + c_4, && (4)
\end{aligned}$$

with a_i, b_i and c_i all being fitting coefficients, θ_0 is a reference temperature, and σ_{s0} is the local sintering stress given by $\sigma_{s0} = 3\alpha/r_0$ with α being the surface tension and r_0 the average grain size. The surface tension and average grain size are assumed to be known and constant such that σ_{s0} is a fitting parameter.

Finally, an evolution equation for the relative density is needed. To this end, conservation of mass provides an expression of the form,

$$\dot{\rho} = -\rho\dot{\varepsilon}_{kk}^{\mathrm{in}}. \tag{5}$$

2.2 Numerical Implementation

As with any 3D constitutive model intended for use with finite element codes, an accurate, robust, and efficient numerical routine is needed. Substantial effort has been made in developing robust return mapping algorithms [14, 15, 16, 17, 18] for plasticity based on

---

[1] The theoretical derivation assumes a two phase system composed of a bulk skeleton and void phase. See Olevsky [10] for details of the theory.

operator splitting [19]. A key feature of such implementations is the separation of the elastic and plastic response. Specifically, in (visco-)plasticity the magnitude of the inelastic, plastic strain increment is given by a consistency parameter (commonly the equivalent plastic strain increment) that is found by enforcement of the consistency relation[2]. Dependence on stress in then brought in through the direction of inelastic deformation and satisfaction of the consistency constraint.

For the current SOVS sintering model, such a separation is not evident. Specifically, through Eqn. 1 it is evident that the direction and magnitude of inelastic strain depends directly on the stress state. Thus, conventional routines like those in the previous citations cannot be used to integrate this model, and a different approach is needed. In the literature and previous versions, the SOVS model was integrated using a "semi-implicit" formulation put forth by McHugh and Riedel [9] that was based on a prior viscoplastic creep implementation of Peirce *et al.* [20]. In the two decades since these efforts, recent work has focused on developing new algorithms for the robust, implicit solution of constitutive models (see [17, 18]). Here both the conventional McHugh and Riedel and a fully implicit integration scheme are described to explore the relative capabilities.

Given the small strain and time-dependent nature of the formulation in the proceeding section a hypoelastic scheme is used. For a constitutive model integrated from $t = t_n$ to t_{n+1}, via loadings of total strain increments $d\varepsilon_{ij} = \varepsilon_{ij}^{n+1} - \varepsilon_{ij}^{n}$ and prescribed temperature steps $d\theta = \theta^{n+1} - \theta^{n}$, the stress may be integrated as,

$$\begin{aligned} \sigma_{ij}^{n+1} &= \sigma_{ij}^{n} + d\sigma_{ij}, && (6)\\ d\sigma_{ij} &= \mathbb{C}_{ijkl}\left(d\varepsilon_{kl} - d\varepsilon_{kl}^{\text{in}}\right), && (7) \end{aligned}$$

with $\mathbb{C}_{ijkl}$ the fourth order stiffness tensor (assumed isotropic). The remaining state variables may be integrated as,

$$\begin{aligned} \varepsilon_{ij}^{\text{in}(n+1)} &= \varepsilon_{ij}^{\text{in}(n)} + d\varepsilon_{ij}^{\text{in}}, && (8)\\ \rho^{n+1} &= \rho^{n} + d\rho. && (9) \end{aligned}$$

where,

$$\begin{aligned} d\varepsilon_{ij}^{\text{in}} &= (1-\beta)\,\dot{\varepsilon}_{ij}^{\text{in}(n)}\Delta t + \beta\dot{\varepsilon}_{ij}^{\text{in}(n+1)}\Delta t, && (10)\\ d\rho &= (1-\beta)\,\dot{\rho}^{n}\Delta t + \beta\dot{\rho}^{n+1}\Delta t, && (11) \end{aligned}$$

---

[2] In rate-independent formulations, this revolves around satisfaction of the yield surface, f, being zero during inelastic deformation ($f(t) = 0$). For viscoplasticity, a variety of similar concepts are invoked.

and $\beta \in [0,1]$ is an integration constant and $\Delta t = t_{n+1} - t_n$. With the values at $t = t_n$ known, the difference in the two approaches is associated with the question of determining the rates at $t = t_{n+1}$.

McHugh-Riedel (MR) Implementation [9]

For the McHugh-Riedel "semi-implicit" approach, the updated rates of stain variable relation are essentially determined by performing a Taylor-series expansion of the terms about their values at $t = t_n$,

$$\begin{aligned} \dot{\varepsilon}_{ij}^{\mathrm{in}(n+1)} &= \dot{\varepsilon}_{ij}^{\mathrm{in}(n)} + \frac{\partial \dot{\varepsilon}_{ij}^{\mathrm{in}}}{\partial \sigma_{kl}} d\sigma_{kl} + \frac{\partial \dot{\varepsilon}_{ij}^{\mathrm{in}}}{\partial \rho} d\rho + \frac{\partial \dot{\varepsilon}_{ij}^{\mathrm{in}}}{\partial \theta} d\theta, & (12) \\ \dot{\rho}^{n+1} &= \dot{\rho}^{n} + \frac{\partial \dot{\rho}}{\partial \sigma_{ij}} d\sigma_{ij} + \frac{\partial \dot{\rho}}{\partial \rho} d\rho + \frac{\partial \dot{\rho}}{\partial \theta} d\theta. & (13) \end{aligned}$$

In this case, the derivates are evaluated at $t = t_n$. Inserting Eqns. 12 and 13 into Eqns. 10 and 11 and using Eqn. 7 produces the following system of equations,

$$\begin{aligned} \mathcal{L}_{ijkl}^{-1} d\sigma_{kl} + \beta \Delta t \frac{\partial \dot{\varepsilon}_{ij}^{\mathrm{in}}}{\partial \rho} d\rho &= d\varepsilon_{ij} - \dot{\varepsilon}_{ij}^{\mathrm{in}(n)} \Delta t - \beta \Delta t \frac{\partial \dot{\varepsilon}_{ij}^{\mathrm{in}}}{\partial \theta} d\theta, & (14) \\ -\beta \Delta t \frac{\partial \dot{\rho}}{\partial \sigma_{ij}} d\sigma_{ij} + \left(1 - \beta \Delta t \frac{\partial \dot{\rho}}{\partial \rho}\right) d\rho &= \dot{\rho}^{n} \Delta t + \beta \Delta t \frac{\partial \dot{\rho}}{\partial \theta} d\theta, & (15) \end{aligned}$$

where,

$$\mathcal{L}_{ijkl}^{-1} = \mathbb{S}_{ijkl} + \beta \Delta t \frac{\partial \dot{\varepsilon}_{ij}^{\mathrm{in}}}{\partial \sigma_{kl}}, \qquad (16)$$

with $\mathbb{S}_{ijkl} = \mathbb{C}_{ijkl}^{-1}$ being the fourth order compliance tensor. Solving for $d\sigma_{ij}$ and $d\rho$ yields,

$$\begin{aligned} d\rho &= \frac{\dot{\rho}^{n} \Delta t + \beta \Delta t \frac{\partial \dot{\rho}}{\partial \theta} d\theta + \beta \Delta t \frac{\partial \dot{\rho}}{\partial \sigma_{ij}} \mathcal{L}_{ijkl} \left(d\varepsilon_{kl} - \dot{\varepsilon}_{kl} \Delta t - \beta \Delta t \frac{\partial \dot{\varepsilon}_{kl}}{\partial \theta} d\theta \right)}{1 - \beta \Delta t \frac{\partial \dot{\rho}}{\partial \rho} + (\beta \Delta t)^2 \frac{\partial \dot{\rho}}{\partial \sigma_{ij}} \mathcal{L}_{ijkl} \frac{\partial \dot{\varepsilon}_{kl}^{\mathrm{in}}}{\partial \rho}}, & (17) \\ d\sigma_{ij} &= \mathcal{L}_{ijkl} \left(d\varepsilon_{kl} - \dot{\varepsilon}_{kl}^{\mathrm{in}(n)} \Delta t - \beta \Delta t \frac{\partial \dot{\varepsilon}_{kl}^{\mathrm{in}}}{\partial \theta} \Delta\theta - \beta \Delta t \frac{\partial \dot{\varepsilon}_{kl}^{\mathrm{in}}}{\partial \rho} d\rho \right). & (18) \end{aligned}$$

Implicit Implementation

A fully implicit approach may be pursued by again considering Eqns. 8-11 but instead of using a Taylor expansion of the rates at $t = t_{n+1}$ an iterative solution technique is used to directly solve for them. To this end, Eqns. 10 and 11 are recast in residual form as,

$$\begin{aligned} r^{\varepsilon}_{ij} &= -d\varepsilon^{\text{in}}_{ij} + (1-\beta)\,\dot{\varepsilon}^{\text{in}(n)}_{ij}\Delta t + \beta\dot{\varepsilon}^{\text{in}(n+1)}_{ij}\Delta t, \qquad (19) \\ r^{\rho} &= -d\rho + (1-\beta)\,\dot{\rho}^{n}\Delta t + \beta\dot{\rho}^{n+1}\Delta t. \qquad (20) \end{aligned}$$

A key to this approach is initializing the various variables appropriately to enable convergence to the solution. In rate-independent elastic-plastic routines, this is typically done in an elastic predictor-inelastic corrector scheme in which all input deformations are assumed to be elastic and initializing all inelastic, plastic terms to their values at the previous converged time-steps (see [21]). Such a scheme is complicated for the current routine due to (i) the loss of complete separation between elastic and inelastic deformations as indicated by Eqn. 1 and (ii) the possibility of substantial inelastic deformation even under low/no-load (as indicated by the verification exercises of [12]). The second point indicates that trial deformations could lead to excessive trial stress necessitating use of line-search [17] or trust-region [18] augmentations of the constitutive routines to achieve convergence. An alternative that could alleviate this issue is to invert the concept and try an "inelastic predictor-elastic corrector" type scheme. In the proposed approach, this concept is achieved by setting,

$$\begin{aligned} \sigma^{(k=0)}_{ij} &= \sigma^{n}_{ij}, \qquad \dot{\varepsilon}^{\text{in}(k=0)}_{ij} = \hat{\dot{\varepsilon}}^{\text{in}}_{ij}\left(\sigma^{(k=0)}_{ij}\right), \qquad (21) \\ d\varepsilon^{\text{in}(k=0)}_{ij} &= d\varepsilon_{ij}, \qquad \rho^{(k=0)} = \rho^{n}, \qquad \dot{\rho}^{(k=0)} = -\rho^{(k=0)}\dot{\varepsilon}^{(k=0)}_{kk}, \qquad (22) \end{aligned}$$

in which k denotes the inelastic correction increment. Some of these selections are debatable given item (i) above. To concretely resolve this issue, some consideration of the initial guesses and impact on convergence properties would likely be needed.

To find the updated material state at $t = t_{n+1}$, the state variables must be incrementally updated until convergence is achieved as measured by sufficient reduction in the residuals. In the current work, a merit function, m, of the form,

$$m = \frac{1}{2}\left(\left(\frac{r^{\rho}}{\rho_0}\right)^2 + \left(\frac{E}{\sigma_{s0}}\right)^2 r^{\varepsilon}_{ij}r^{\varepsilon}_{ij}\right), \qquad (23)$$

is used to assess convergence. Here, E is the elastic modulus, and ρ_0 is the initial relative density. Specifically, $\sqrt{m}$ is used as a convergence criteria. This form represents a scaled, unweighted merit function that simultaneously assesses performance of both residuals instead of separate tolerances. The scaling coefficients, $1/\rho_0$ and E/σ_{s0}, are introduced to ensure equal contribution of both residuals to the merit function. The selection and impact of these coefficients for elastic-plastic models has been explored in [18].

To iterate and find the solution, a standard Newton-Raphson scheme is used in which increments of the state variables are found by solving the system of equations formed when linearizing the residuals in terms of the solution variables (see [22]). This approach results in a system of equations as,

$$
\begin{aligned}
-r_{ij}^{\varepsilon(k)} &= \mathcal{L}_{ijkl}^{-1}\Delta\sigma_{kl} + \beta\Delta t\frac{\partial\dot{\varepsilon}_{ij}^{\text{in}}}{\partial\rho}\Delta\rho, && (24)\\
-r^{\rho(k)} &= \beta\Delta t\frac{\partial\dot{\rho}}{\partial\sigma_{ij}}\Delta\sigma_{ij} + \left(-1+\beta\Delta t\frac{\partial\dot{\rho}}{\partial\rho}\right)\Delta\rho, && (25)
\end{aligned}
$$

where $\Delta\sigma_{ij}$ and $\Delta\rho$ are increments in stress and relative density, respectively, such that,

$$
\begin{aligned}
\sigma_{ij}^{k+1} &= \sigma_{ij}^{k} + \Delta\sigma_{ij}^{k}, && (26)\\
\rho^{k+1} &= \rho^{k} + \Delta\rho^{k}. && (27)
\end{aligned}
$$

The various derivatives and terms are evaluated using updated state terms rather than previously converged values. Solving the system comprised of Eqns. 24 and 25 yields,

$$
\begin{aligned}
\Delta\rho &= \frac{-r^{\rho} + \beta\Delta t\frac{\partial\dot{\rho}}{\partial\sigma_{ij}}\mathcal{L}_{ijkl}r_{kl}^{\varepsilon}}{-1+\beta\Delta t\frac{\partial\dot{\rho}}{\partial\rho} - (\beta\Delta t)^2\frac{\partial\dot{\rho}}{\partial\sigma_{ij}}\mathcal{L}_{ijkl}\frac{\partial\dot{\varepsilon}_{kl}^{\text{in}}}{\partial\rho}}, && (28)\\
\Delta\sigma_{ij} &= -\mathcal{L}_{ijkl}\left(r_{kl}^{\varepsilon} + \beta\Delta t\frac{\partial\dot{\varepsilon}_{kl}^{\text{in}}}{\partial\rho}\Delta\rho\right). && (29)
\end{aligned}
$$

3 Results

To assess the capabilities of the formulations and assess the impact of the proposed fully implicit schemes, the constitutive verification and bilayer bar structural verification exercises used by Argüello *et al.* [12] are studied. The former is presented in Section 3.1 while the latter is investigated in Section 3.2. For both studies, the "Continuum Mechanics" set of model parameters corresponding to 0.2μm ZnO power given by Argüello *et al.* [12] (originally coming from [10]) are used. The model parameters are given in Table 1 while $E = 123.7$ GPa and a Poisson ratio, ν, of $\nu = 0.356$ is used.

For these studies, both the McHugh-Riedel (denoted "MR") and new implicit approach (referred to as "New" in following for convenience) were implemented in the Sierra/SolidMechanics [23]. All simulations were then performed with Sierra/SolidMechanics.

a_1	1 (-)	b_1	2 (-)		
a_2	2/3 (-)	b_2	3 (-)	c_2	1 (-)
a_3	1 (-)	b_3	2 (-)		
a_4	517 (GPa-s)	b_4	-1066 (GPa-s)	c_4	564 (GPa-s)
α	1.27 (J/m^2)	r_0	1 (μm)		

Table 1: SOVS Model Parameters [10, 12] for a 0.2μm ZnO powder used in this work

3.1 Constitutive Verification

As a first step to verify the constitutive implementation, the verification exercises of Argüello *et al.* [12] are considered. These exercises comprise of two problems: *free-sinter* and *sinter-forge*. The first problem corresponds to a no-load condition with a prescribed temperature profile while the second is associated with the same temperature history but with a constant 1 MPa tensile load. For both problems, the assumed temperature profile is that of a constant linear ramp from $\theta\,(t=0) = 750°\mathrm{C}$ to $\theta\,(t=t_f) = 1000°\mathrm{C}$ at a constant ramp rate of $5\frac{°\mathrm{C}}{\mathrm{min}}$ such that $t_f = 3000$ s. In the following, these problems are simulated with a single finite element to eliminate any impacts of a structural problem and test the specific constitutive implementation.

For the free-sinter case, by assuming no-load ($\sigma_{ij} = 0$) and using Eqns. 1 and 5 while substituting expressions Eqns. 2–4 the rate of change of the density may be written,

$$\dot{\rho} = \frac{a_3 \sigma_{s0}}{2 a_2 \eta_0} \rho^{b_3 - b_2 + 1} \left(1-\rho\right)^{c_2}, \tag{30}$$

which with parameters given in Table 1 yields the simplified expression for normalized porosity, $\xi = 1 - \rho$,

$$\dot{\xi} = -\frac{3\sigma_{s0}\xi}{4\eta_0}, \tag{31}$$

that can be analytically integrated in time by the solution given by Argüello *et al.* [12]. For the sinter-forge case, no analytical solution may be found. As such, the normalized porosity is numerically integrated[3] via [12],

$$\dot{\xi} = \frac{\sigma\xi}{4\eta_0\left(1-\xi\right)^2} - \frac{3\sigma_{s0}\xi}{4\eta_0}, \tag{32}$$

where σ is the applied uniaxial stress (1 MPa tensile load for the given case).

---

[3] A simple forward Euler scheme is used with $\Delta t = 0.6$s.

Results of the verification exercises presenting the evolution of the relative densities with temperature are given in Fig. 1 for both the free-sinter and sinter-forge cases using the McHugh-Riedel (MR) and new implicit (New) implementation with $\beta = 1.0$. Two temporal discretizations are considered; one coarse with 5 uniform time steps corresponding to $\Delta t =$ 600s and one fine of 200 uniform time steps with $\Delta t = 15$ s. From the results of Fig. 1 it can be seen that with the smaller time steps (Fig. 1b) both formulations reproduce the (semi-) analytical formulations very well, while differences are noted at the coarser scale (Fig. 1a). With respect to the larger time steps for the new implicit implementation, the actual density is always lower than the analytical forms, while in the case of the McHugh-Riedel model the relative density is initially greater before crossing the reference solution and ending up with a smaller relative density.

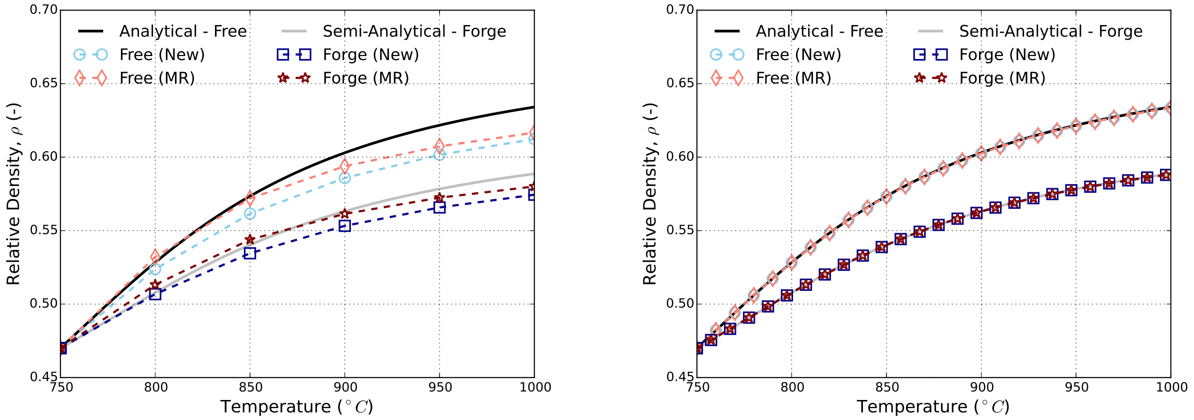

(a) $\Delta t = 600$s (b) $\Delta t = 15$s

Figure 1: Evolution of the relative density, ρ, through the free-sinter and sinter-forge problems with loading increments of (a) $\Delta t = 600$s and (b) $\Delta t = 15$s. Numerical results with both the McHugh-Riedel (MR) and new implicit implementation (New) are presented. In all cases, $\beta = 1.0$.

To further consider the impact of the time step size on performance, convergence studies for both the free-sinter (Fig. 2a) and sinter-forge (Fig. 2b) problems are presented in Figure 2. Results for both the McHugh-Riedel and implicit scheme are presented with $\beta = 0.5$ and $\beta = 1.0$. The relative error considered in these studies is in terms of the *final* relative density of the numerical results versus the reference, (semi-) analytical results. It is important to highlight that the error is not integrated over loading and merely reflects the final state. Nonetheless, for the current discussion the use of this metric seems more than sufficient to discuss the relative performance.

From the results of Fig. 2, it may be observed that the behaviors of the two problems are very similar. Specifically, error decreases with time-step size (as would be expected) and in general the $\beta = 1.0$ cases have errors that are higher than $\beta = 0.5$. This difference can be attributed to what is essentially numerical error in integrating the response through time.

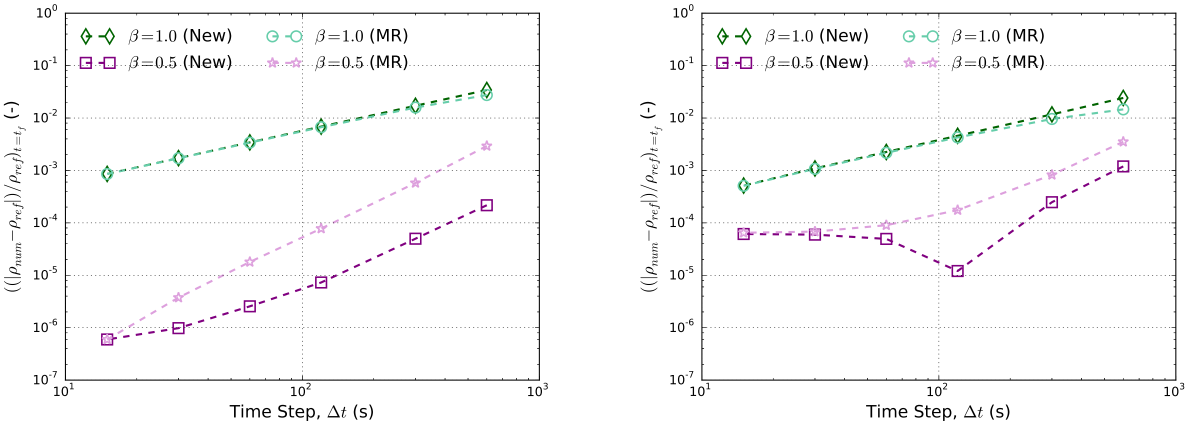

(a) Free-sinter (b) Sinter-forge

Figure 2: Error convergence of the (a) free-sinter and (b) sinter-forge in terms of time step size. Error is given in terms of the relative difference of the *final* relative density to the (semi-) analytical references. Results for the new implicit (New) and McHugh-Riedel (MR) numerical schemes are given with $\beta = 0.5,\ 1.0$.

Along this line, in the results of Fig. 1 it can be seen that the densification rate ($\dot{\rho}$) *decreases* through loading. As such, with $\beta = 1.0$, $d\rho$ will leverage this lower end-of-step rate yielding lower relative densities. This fact is reflected in the new implicit results of Fig. 1a in which the numerically determined density is continually lower than the reference solutions. In comparing the performance of the semi-implicit McHugh-Riedel implementation and those of the new implicit scheme, little difference can be noted with $\beta = 1.0$. Some small decrease in the final error can be noted at larger time-steps with $\beta = 1.0$ but the differences are small and by considering Fig. 1a this may be potentially be associated with choise of error metric. When $\beta = 0.5$, the new implicit scheme shows smaller errors than the existing McHugh-Riedel implementation for both the free-sinter and sinter-forge and all time-steps. In fairness, the errors of either implementation are small.

3.2 Bilayer Bar

With the constitutive implementations verified in Section 3.1, the next step is to assess performance for structural problems. To this end the bilayer bar problem of Argüello *et al.* [12] is used. Note that slightly different geometries and parameter sets were used for purposes of verification and validation in the work of [12]. Here as the numerical implementation and not model form, is of interest, the previous validation is still applicable. Thus, only the geometry corresponding to the verification exercises is considered, and the only parameter set used is that of Table 1. It should also be pointed out that while Argüello *et al.* [12] detail modifications to JAS3D needed to assess global convergence of this problem given the lack of external loading, no such issues/modifications were needed for the current study.

Conceptually, the bilayer bar problem is very similar to the classic bimaterial strip example.

Specifically, a bar comprised of two sections of the same material, but different initial relative densities, is uniformally heated. The solidification problem produces different contractions in the two layers leading to a macroscopic bending. Although no-load conditions are maintained on the exterior of the specimen, the variable material state will produce stresses along the interface and interior. For the current study, $\rho_0^{\text{upper}} = 0.47$ and $\rho_0^{\text{lower}} = 0.57$ and the same thermal profile as in the verification studies is used ($\theta\,(t = 0) = 750°\text{C} \rightarrow \theta\,(t = 3000s) = 1000°\text{C}$ at a constant ramp rate of $5\frac{°\text{C}}{\text{min}}$).

The bilayer bar geometry is schematically represented in Fig. 3. Specific dimensions are taken from [12] and are $L = 7$ mm, $W = 4$ mm, and $H_u = H_l = 1.125$ mm such that $H = 2.250$ mm. The unit vectors $\hat{e}_x$, $\hat{e}_y$, and $\hat{e}_z$ correspond to directions X, Y, and Z while three points (pts. 2, 4, and 6) are marked in Fig. 3 and correspond to points used by Argüello *et al.* [12] whose displacements (in the Z direction) were quantities of interest. Given the lack of external load and geometry, quarter symmetry is used in this problem. Specifically, only the darker shaded quarter in Fig. 3 is meshed and modeled. Symmetry conditions in the $\hat{e}_z$ and $\hat{e}_x$ were imposed on the respective planes while a single node (at bar center along the bottom edge) is fixed in the through thickness ($\hat{e}_y$) direction to prevent the corresponding rigid body mode.

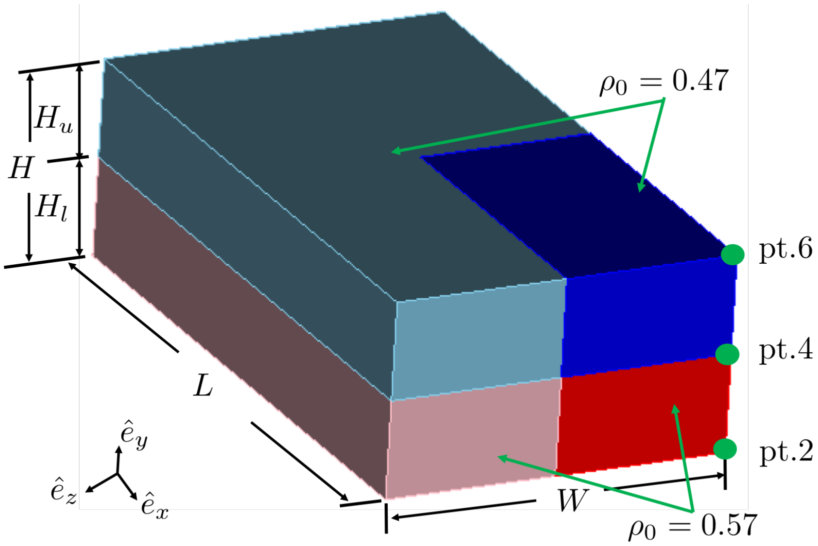

Figure 3: Schematic of the bilayer bar problem geometry.

To study the impact of spatial and temporal discretizations, a series of meshes were constructed and then simulated with a variety of time-step sizes. To create the different meshes, the desired number of elements in the through thickness direction was specified and the characteristic mesh size was then determined by the total height (H) divided by the desired number of elements. This dimension was used as a nominal mesh size and the entire geometry was seeded with uniform hex elements. In what follows, the different meshes will be referred to by the nominal number of through thickness elements. Meshes were constructed with 8, 12, 20, and 32 through thickness elements corresponding to models with 672, 2,508, 11,160, and 44,800 elements, respectively. Selective deviatoric [23] elements were used. The four meshes were each simulated with six different time discretizations involving different number of fixed, uniform time-steps. Specifically, time-steps of $\Delta t = 15$, 30, 60, 120, 300 and 600 s were used corresponding to simulations with 200, 100, 50, 25, 10, and 5 uniform loading steps. For use as a reference comparison in later discussions, the problem was also run using a 36 through thickness element mesh (64,512 elements) and 400 evenly spaced increments of $\Delta t = 7.5$s. For the reference case, a fully implicit case of $\beta = 1.0$ was used.

Convergence

The ability of the coarse meshes to reproduce results of the fine discretizations is considered in Fig. 4. This comparison is made by investigating the macroscopic quantities of interest used by Argüello *et al.* [12]; namely the displacements in the $\hat{e}_z$ direction, denoted w, at nodes 2, 4, and 6. These results are given for the coarse mesh (8 through-thickness elements) with time-steps of $\Delta t = 600$s and $\Delta t = 15$s along with the reference simulation. Figures 4a and 4c presents the results for the legacy McHugh-Riedel implementation with $\beta = 0.5$ and $\beta = 1.0$, respectively, while the complementary results with the new scheme are given in Figs. 4b and 4d. From these results, it may be observed that in all cases good accuracy is obtained with $\Delta t = 15$ s. For the coarser time scale, $\Delta t = 600$ s, the new implementation with $\beta = 0.5$ shows similar level accuracy levels to the fine time scale. The other three cases, however, all show substantial error with this reduced number of time-steps. As with the previous constitutive verifications, the new implementation at $\beta = 1.0$ underpredicts the final deformation. The existing McHugh-Riedel implementation results for $\beta = 0.5$ and 1.0 both produce final displacements approximately 10% higher than the reference case.

To consider the convergence characteristics of the two algorithms more concretely, Fig. 5 presents a time-convergence study for the two different implementations at $\beta = 0.5$ and 1.0 for the 8-through thickness element cases. Error is assessed in terms of the relative difference of the final displacement in the $\hat{e}_z$ direction of node 6 (w_6) versus the reference case. From Fig. 5 it is clear that the "New" implementation, with either β, shows superior convergence characteristics versus that of the legacy McHugh-Riedel. As would be expected from Fig. 4, the $\beta = 0.5$ cases demonstrate substantially better accuracy than their counterparts at larger time-steps. Improvement with increasing number of load increments, however, eventually saturate and at the $\Delta t = 30$ s case the $\beta = 1.0$ case overtakes $\beta = 0.5$.

Figures 4 and 5 highlight the capabilities of the two implementations to capture the deformation fields. These results, however, do not provide any information on the stress fields; another important result in any mechanical analysis. To this end, Fig. 6 presents the average stress in the $\hat{e}_x$ direction for the top and bottom layers indicated in Fig. 3. Although generally similar results were obtained with respect to the deformation fields between the numerical formulations, vastly different responses are noted in Fig. 6. With $\beta = 1.0$ (Figs. 6c and 6d), similar responses can be noted. Specifically, the new implementation converges for all of the different time-steps to very similar average stress levels. The existing McHugh-Riedel formulation converges towards comparable stress levels but larger number of load increments are needed to achieve those values. The $\beta = 0.5$ cases, on the other hand, exhibit

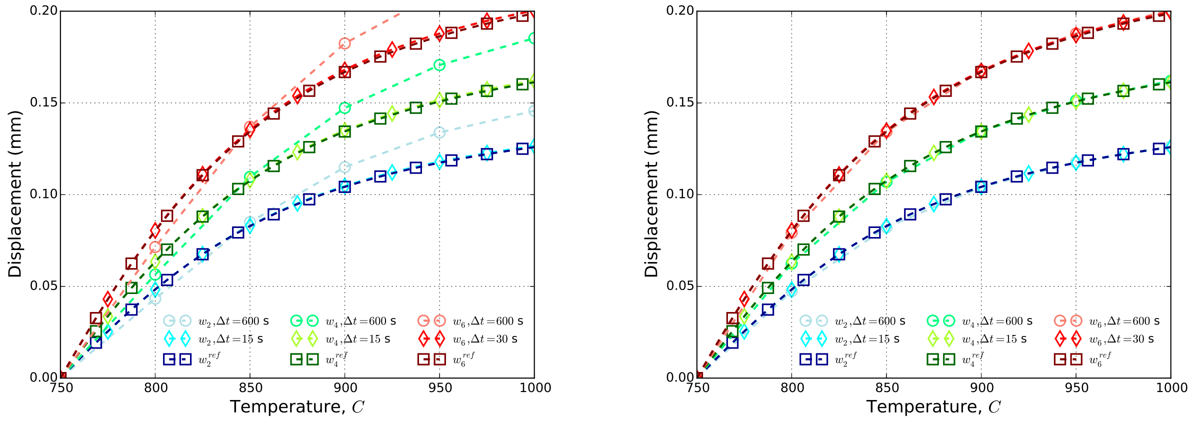

(a) McHugh-Riedel, $\beta = 0.5$ (b) New, $\beta = 0.5$

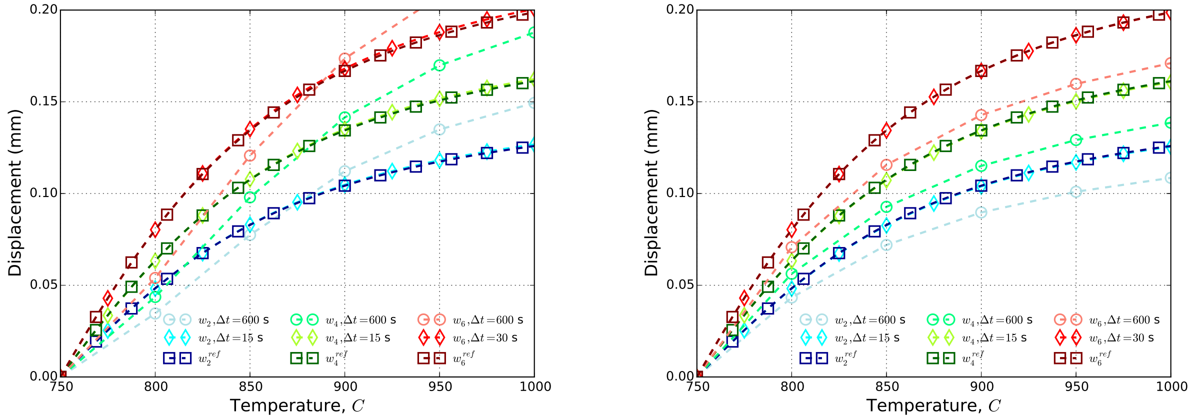

(c) McHugh-Riedel, $\beta = 1.0$ (d) New, $\beta = 1.0$

Figure 4: Evolution of the edge displacements noted in Fig. 3 through the sintering process using the (a,c) McHugh-Riedel and (b,d) new implicit scheme with $\Delta t = 600$ and 15 s and (a,b) $\beta = 0.5$ and (c,d) $\beta = 1.0$. For comparison, results from a reference fine-meshed, small time-step simulation are also presented.

substantial oscillations and unstable (the new implementation in Fig. 6b) and what seems to be conditionally stable (McHugh-Riedel, Fig. 6a) responses. In both cases, these issues are mitigated with decreased time-step sizes but at the finest presented cases ($\Delta t = 7.5$ s) oscillatory behaviors are still clearly present.

Such oscillatory responses have been previously noted with time-dependent creep and viscoplastic formulations and are associated with the stability of the time-integration of the constitutive formulation [24, 25, 26]. The original work of Pierce *et al.* [20] noted stable responses for $\beta \geq 0.5$ for their creep formulation and contextualized their observations based on the analysis of Zienkiewicz and Cormeau [24] and Cormeau [25]. McHugh and Riedel [9] built upon these observations in their formulation and stated that they exhibited improved

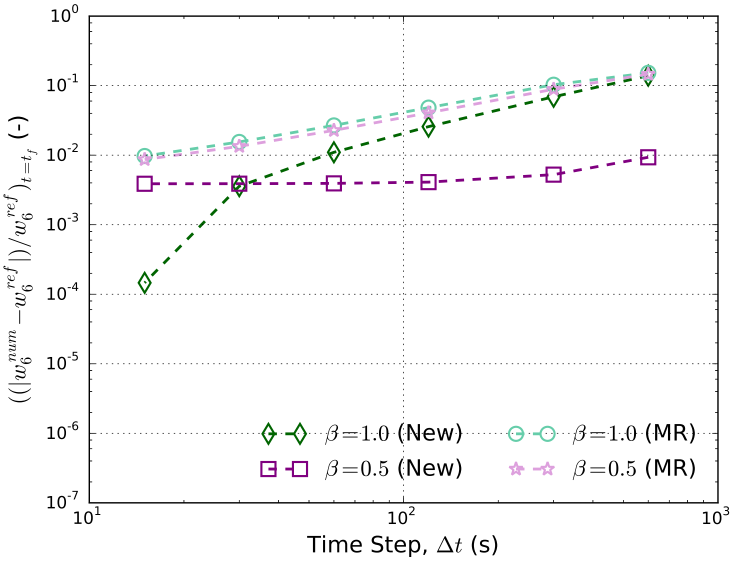

Figure 5: Temporal convergence of the bilayer bar problem with the 8 element through-thickness mesh with different numerical formulations.

accuracy with $\beta = 0.5$ instead of $\beta = 0.0$. It must be pointed out that both the viscoplastic models [20, 25] and liquid-state sintering model of McHugh-Riedel [9] have different formulations from each other and the current viscous sintering model making the applicability of the previous stability analysis unknown. In their investigation of the SOVS model, Argüello *et al.* [12] do not comment on the selected integration parameter. Additionally, neither the previous reports of McHugh and Riedel [9] or Argüello *et al.* [12] report on the mechanical stress fields. Thus, whether or not these issues have been observed before is unknown.

In terms of the relative magnitudes, the stress values observed in all of the results of Fig. 6 are fairly small ($\approx <$ .1 MPa). However, the differences of the free-sinter and sinter-forge cases in Fig. 1 demonstrate that even seemingly small stress values can impact the deformation response and highlight the importance of resolving and capturing both the relative density and stress fields to accurately predict the results of a sintering process. Therefore, even though the $\beta = 0.5$ simulations in Fig. 2 exhibit improved accuracy at larger time-steps, the corresponding instability in the stress fields mean such integration is not desirable. The $\beta = 1.0$ case does not exhibit such numerical stability problems and acceptable accuracy. As such, the integration parameter $\beta = 1.0$ is used in the remainder of this work and addressing and analyzing the numerical stability is left to future efforts.

Bearing the choice of integration parameter $\beta = 1.0$ in mind, Fig. 7 investigates mesh convergence and the impact of spatial discretization. Essentially, time convergence studies like those presented in Fig. 5 are repeated for each mesh using the McHugh-Riedel (Fig. 7a) and new (Fig. 7b) schemes. In general, lower errors and faster rates of convergence are noted for the new implicit scheme versus than existing McHugh-Riedel implementation. At larger

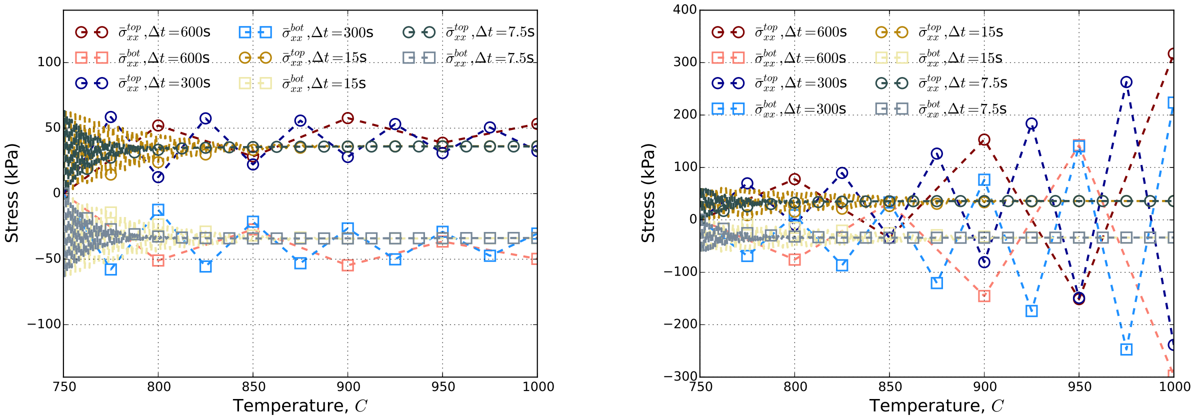

(a) McHugh-Riedel, $\beta = 0.5$ (b) New, $\beta = 0.5$

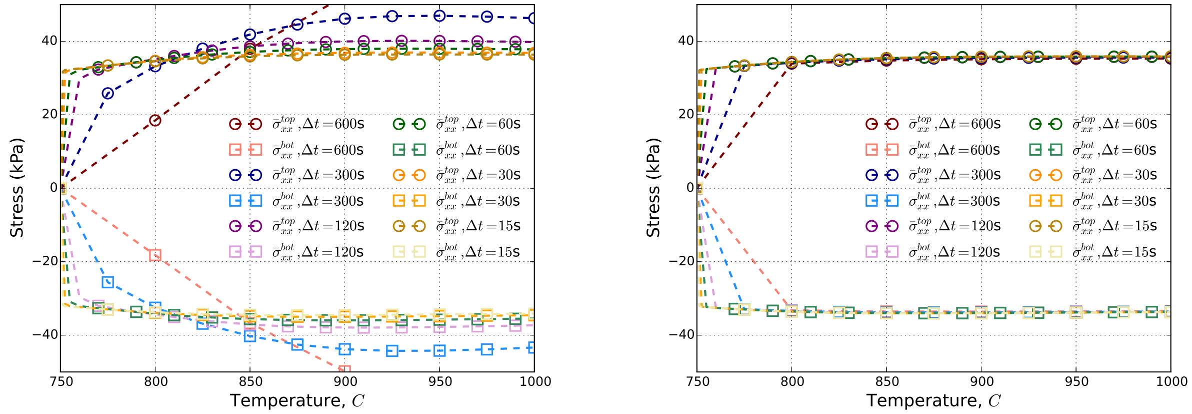

(c) McHugh-Riedel, $\beta = 1.0$ (d) New, $\beta = 1.0$

Figure 6: Evolution of the average stress in the top and bottom layers, $\bar{\sigma}_{xx}^{\text{top}}$ and $\bar{\sigma}_{xx}^{\text{top}}$, respectively, through the sintering process using the (a,c) McHugh-Riedel and (b,d) new implicit scheme and (a,b) $\beta = 0.5$ and (c,d) $\beta = 1.0$ using different time scales. Note, the $\beta = 0.5$ results use a different vertical axes to highlight their behaviors.

time-steps, little impact on mesh size is seen with either approach. For the McHugh-Riedel case, this trend is observed over all time-steps and the final displacement measure seems fairly independent of mesh size. Below $\approx \Delta t = 30$ s some deviation between the convergence of the different meshes is observed for the implicit results. Taken together, these results indicate that potentially more involved error convergence metrics (*e.g.* an energy norm) may be needed to more quantitatively assess the convergence rates of the different schemes. Nonetheless, by comparing the two results it is clear that (*i*) a lower level of error may be achieved by the new scheme for a given spatial and temporal discretization and (*ii*) the limited mesh size dependence indicates that global deformation metrics can be computed by reasonable meshes and time-steps.

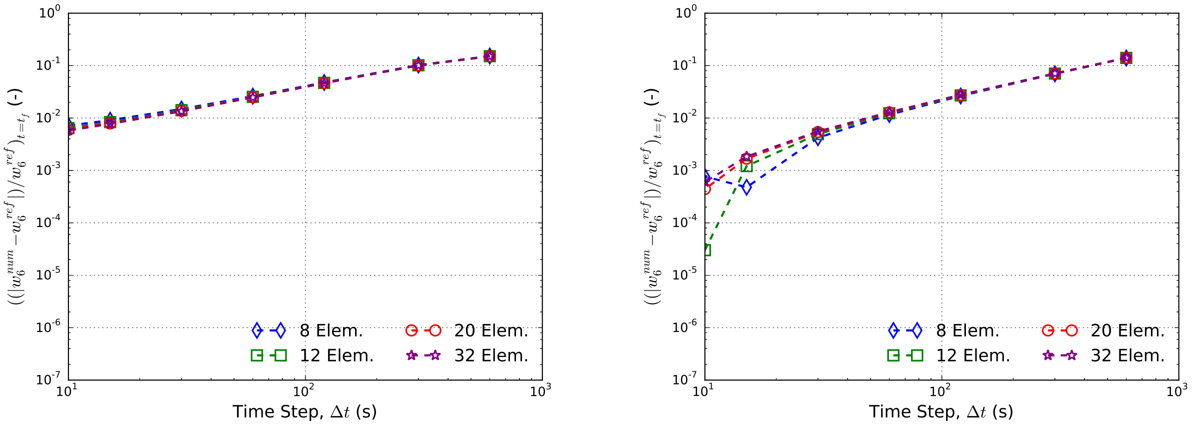

(a) McHugh-Riedel (b) New

Figure 7: Evolution of the edge displacements noted in Fig. 3 through the sintering process using the (a) McHugh-Riedel and (b) new implicit scheme with $\Delta t = 600$ and 15 s and $\beta = 1.0$. For comparison, results from a reference fine-meshed, small time-step simulation are also presented.

The previous convergence studies examine the capabilities of the model and its implementation to resolve global quantities of interest. Such investigations, however, do not reveal anything about the ability of these formulations to resolve spatial variations and corresponding details. To this end, Fig. 8 presents field variations of the reference solution and simulations using the coarse mesh with a large and small time step ($\Delta t = 600$ and 10 s respectively). Only the quarter of the bilayer bar that is simulated is presented in Fig. 8 to enable seeing the field resolution through the cross-section and enable a closer look at the results. Specifically, the relative density, σ_{xx}, and v (displacement in the vertical, $\hat{e}_y$ direction) are shown at the end of the simulation. In terms of the stress, although detail is lost due to the more limited spatial discretization, both the 8 element mesh solutions do a reasonable job of capturing the stress field in comparison to the reference case. For the relative density and displacement, a similar statement can be made for the fine time-scale mesh. Differences can be observed in the displacement and relative density fields when the large time-step is used. Thus, based on these results it would seem that (i) details of state variable fields can be resolved by coarse meshes but (ii) using appropriate temporal discretizations is necessary to accurately resolve these fields.

Timing and Scaling

The current proposed integration scheme is focused on introducing a implicit routine of the constitutive model that relies upon an iterative solution. The existing McHugh-Riedel approach, while "semi-implicit" in construction, leverages a single step solve to find the solution variables. Although the previous results highlight the utilization of an implicit scheme may improve accuracy of the simulation, changing the approach like this is liable to drive up computational cost. To consider this impact, Fig. 9 presents the relative cost

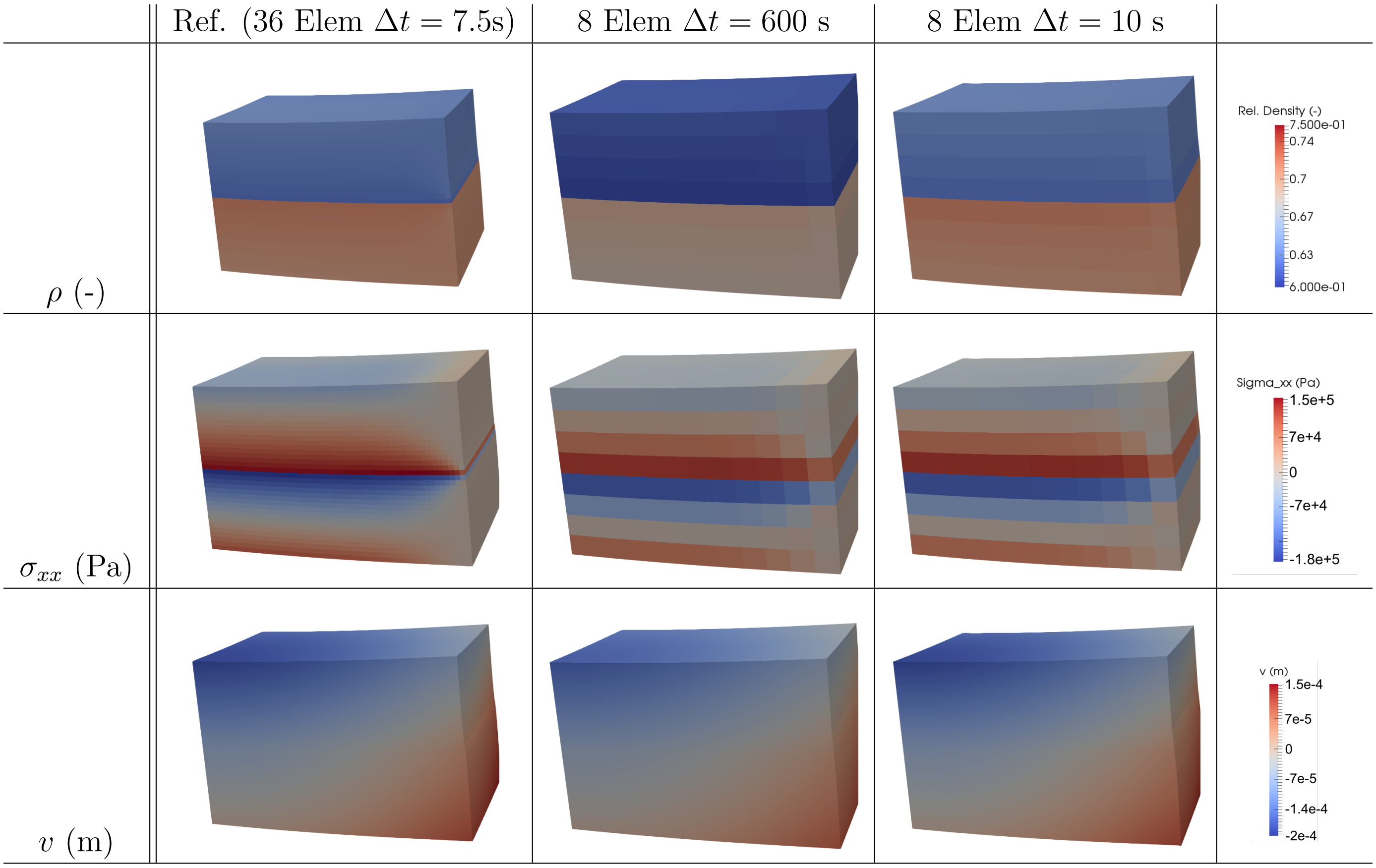

Figure 8: Contour plots of fields of ρ (relative density), σ_{xx} (stress), and v ($\hat{e}_y$ displacement) for the reference model and 8 element through thickness mesh at a coarse ($\Delta t = 600$s) and fine ($\Delta t = 10$ s) temporal discretization. The results of only the quarter symmetry mesh are shown to highlight the internal fields. For reference, the out of plane direction is $\hat{e}_z$ and $\hat{e}_x$ is the horizontal direction (positive pointed to the right).

of the McHugh-Riedel formulation versus the proposed implicit scheme for the 8 element through-thickness mesh with different time-steps. Note, in the results of Fig. 9, the relative time of any case is computed by taking the wall-clock time of the specified formulation and normalizing by its new implicit counterpart. Thus, the normalization times vary with time-step but not across models.

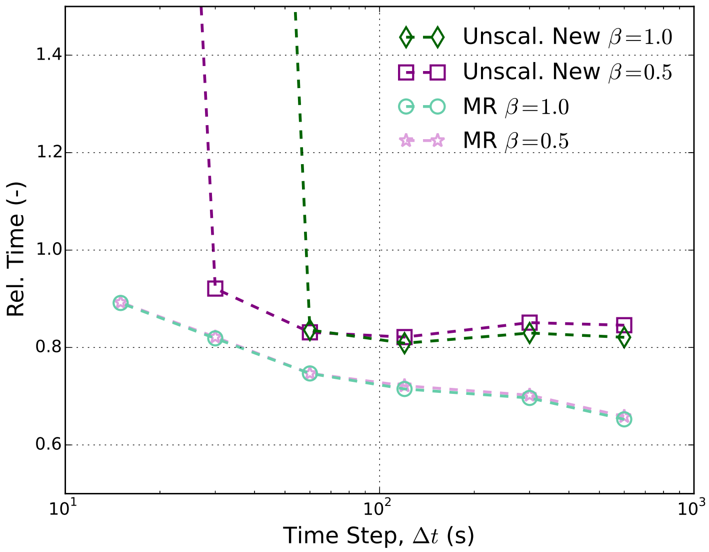

Figure 9: Relative timings of the 8 element through thickness problem at different time-steps. The relative times correspond to the wallclock time of the specified case normalized by the time of the "New", scaled, $\beta = 1.0$ at the corresponding time-step. "Unscal." refers to cases with an unscaled merit function.

From Fig. 9, it is observed that as expected the McHugh-Riedel formulation is faster than the proposed scheme. At larger time-steps, the speed-up is more than 30% while the impact decreases with increasing temporal resolution and at the smallest time-step the timing increase is only ≈ 10%. Although faster, from Fig. 7, it may be noted that this 10% speed-up at $\Delta t = 15$ s also comes with error that is approximately an order of magnitude greater. Thus, the trade-off between speed-up and accuracy is clear. These results seem independent of choice of integration parameter, β.

In Section 2.2 it was mentioned that convergence of the material model was assessed via a scaled merit function. This scaling was introduced to normalize the relative contributions of the two residuals but also, given the choice of terms, has an added effect of essentially tightening the convergence criteria versus an unscaled form for a specified tolerance. The impact of this convergence tightening is also investigated in which the results of using an unscaled merit function[4] are also presented in Fig. 9. At larger time-step cases, the imposed

---

[4] To be clear, $m^{\text{unscaled}} = (1/2)\left((r^\rho)^2 + r^\varepsilon_{ij} r^\varepsilon_{ij}\right)$.

tighter tolerances means additional iterations are needed to converge in the material model. For the global simulation time, these additional computations manifest as increased wallclock time and slower performance. In these cases, ≈20% time savings could be realized by using an unscaled merit function. Below $\Delta t = 60$ s, different behaviors are noted and much increased simulation times are needed for convergence.

A possible explanation of the results for the unscaled merit function in Fig. 9 is associated with the fact that, in essence, the unscaled merit function has a looser convergence criteria than the form of Eqn. 23. If the tolerance is too loose, the constitutive integrator may return unconverged, incorrect stress values that make satisfying global equilibrium more difficult. Such problems, in turn, would require additional global, finite-element iterations and increase cost. Such an issue could be exacerbated by smaller time-steps and corresponding loadings. To consider this issue further, Fig. 10 considers the performance of the constitutive model with different constitutive tolerances. In all previous cases, for both scaled and unscaled merit functions, a tolerance of 1×10^{-9} was used. Figure 10a presents relative timings (normalized to the 1×10^{-9} tolerance case) using decreasing convergence criteria. It can be observed that for tolerances greater than 1×10^{-5}, some small timing improvements may be noted. The drastic cost increases of Fig. 9, however, are not apparent in those cases but do appear when the tolerance is 1×10^{-5}; loosely supporting the previous explanation for the large relative time increases. Even with the larger relative timings, Fig. 10b presents time-step convergence studies like those in Fig. 7 and no dependence of the solution quantity on convergence tolerance is noted.

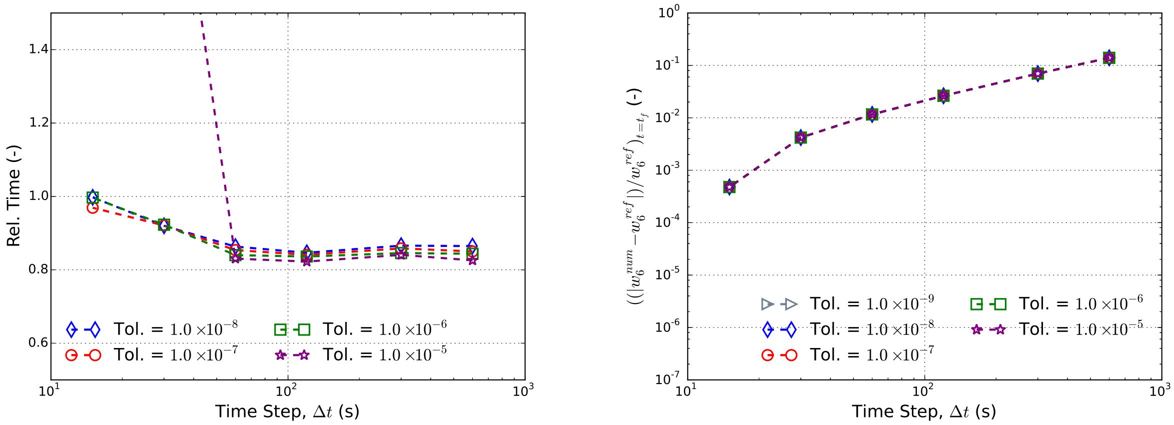

(a) Relative Timings

(b) Time convergence with 8 element through thickness mesh

Figure 10: Impact of constitutive model convergence tolerance on (a) relative simulation time and (b) time-step convergence for the “New” integration scheme with $\beta = 1.0$.

4 Conclusion

Continuum constitutive sintering models are needed to predict the response of different geometries through the sintering process. As such, efficient and accurate implementations of these models represent a potent tool for the design and analysis of corresponding manufacturing stages. One common example of this class of macroscale phenomenological sintering formulation is the Skorohod-Olevsky viscous sintering (SOVS) model. Existing numerical implementations rely on a semi-implicit scheme developed for a liquid-stage sintering model of McHugh-Riedel [9]. A fully implicit scheme represents a potentially enabling capability by increasing accuracy while reducing cost by requiring lower temporal and spatial discretization of global boundary value problems.

Such an implicit scheme was proposed and implemented here. Verification of the model was performed via simple constitutive-level problems and improved accuracy was noted versus the comparable existing implementation. The bilayer bar problem of Argüello *et al.* [12] was then revisited and the performance of both the existing and new implementations was investigated. Through such exercises, it was shown that the new implicit scheme can resolve both global deformation and detailed field responses with reasonable mesh and time-step discretizations. Importantly, these efforts demonstrated that the sintering process can be captured with affordable simulation cost.

With respect to performance, the new implicit scheme shows improved accuracy, in terms of both deformation and stress, versus the previous semi-implicit approach. The increased fidelity does come with higher computational costs of ≈10-30%. Given the improvement in accuracy, however, the longer simulation times are deemed acceptable. Achieving such performance necessitates using a backward Euler integration scheme in time reflected via an integration parameter of $\beta = 1.0$. Results presented here showed that although deformation may be resolved with a value of $\beta = 0.5$, unstable, oscillatory responses in stress were noted that are not only undesirable but also non-physical. As such, only the use of $\beta = 1.0$ can be recommended until additional investigations on the stability properties of the integration scheme can be undertaken and implemented.

Bearing these results in mind, improvements in both physical fidelity and numerical efficiency may be achieved through additional studies. With respect to the former, a variety of extensions to the SOVS model have been proposed incorporating Arrhenius' type temperature dependence in the viscosity and/or introduction of the grain size as a variable (*e.g.* [11, 12]). In terms of the latter, investigating and understanding the stability issue could enable optimal selection of integration parameters for accuracy and help in selecting appropriate spatial and temporal discretizations. Similarly, rigorous convergence studies of different boundary value problems using energy norms could further such understanding. Regardless, the current work represents an important first step in implementing macroscale constitutive models essential for sintering.

Acknowledgements

Sandia National Laboratories is a multimission laboratory managed and operated by National Technology and Engineering Solutions of Sandia, LLC., a wholly owned subsidiary of Honeywell International, Inc., for the U.S. Department of Energy's National Nuclear Security Administration under contract DE-NA0003525.

Bibliography

[1] M. N. Rahaman, Sintering of Ceramics, CRC Press, Boca Raton, FL, 2008.

[2] T. Kraft, H. Riedel, Numerical simulation of solid state sintering; model and application, Journal of the European Ceramic Society 24 (2004) 345–361.

[3] M. Reiterer, T. Kraft, H. Riedel, Manufacturing of a gear wheel made from reaction bonded alumina – numerical simulation of the sinterforming process, Journal of the European Ceramic Society 24 (2004) 239–246.

[4] C. Maruccio, P. Bene, A. Gerardi, D. Bardaro, Integration of CAD, CAE, and CAM procedures for ceramic components undergoing sintering, Journal of the European Ceramic Society 36 (2016) 2263–2275.

[5] M. W. Reiterer, K. G. Ewsuk, An analysis of four different approaches to predict and control sintering, Journal of the American Ceramic Society 92 (7) (2009) 1419–1427. doi:10.1111/j.1551-2916.2009.03009.x.

[6] V. Tikare, M. Braginsky, E. A. Olevsky, Numerical simulation of solid-state sintering: I, sintering of three particles, Journal of the American Ceramic Society 86 (1) (2003) 49–53.

[7] M. Braginsky, V. Tikare, E. Olevsky, Numerical simulation of solid state sintering, International Journal of Solids and Structures 42 (2005) 621–636.

[8] E. A. Olevsky, V. Tikare, T. Garino, Multi-scale study of sintering: a review, Journal of the American Ceramic Society 89 (6) (2006) 1914–1922. doi:10.1111/j.1551-2916.01054.x.

[9] P. E. McHugh, H. Riedel, A liquid phase sintering model: application to Si_3N_4 and WC-Co, Acta Materialia 45 (7) (1997) 2995–3003.

[10] E. A. Olevsky, Theory of sintering: from discrete to continuum, Materials Science and Engineering R23 (1998) 41–100.

[11] M. W. Reiterer, K. G. Ewsuk, J. G. Argüello, An Arrhenius-type viscosity function to model sintering using the Skorohod-Olevsky viscous sintering model within a finite-element code, Journal of the American Ceramic Society 89 (6) (2006) 1930–1935. doi:10.1111/j.1551-2916.01041.x.

[12] J. G. Argüello, M. W. Reiterer, K. G. Ewsuk, Verification, performance, validation, and modifications to the SOVS continuum constitutive model in a nonlinear large-deformation finite element code, Journal of the American Ceramic Society 92 (7) (2009) 1442–1449.

[13] T. T. Molla, D. W. Ni, R. Bulatova, R. Bjørk, C. Bahl, N. Pryds, H. L. Frandsen, Finite element modeling of camber evolution during sintering of bilayer structures, Journal of the American Ceramic Society 97 (9) (2014) 2965–2972. doi:10.1111/jace.13025.

[14] M. Ortiz, E. P. Popov, Accuracy and stability of integration algorithms for elastoplastic constitutive relations, International Journal for Numerical Methods in Engineering 21 (1985) 1561–1576.

[15] M. Ortiz, J. C. Simo, An analysis of a new class of integration algorithms for elastoplastic constitutive relations, International Journal for Numerical Methods in Engineering 23 (1986) 353–365.

[16] A. Pérez-Foguet, F. Armero, On the formulation of closest-point projection algorithms in elastoplasticity – part II: Globally convergent schemes, International Journal for Numerical Methods in Engineering 53 (2002) 331–374.

[17] W. M. Scherzinger, A return mapping algorithm for isotropic and anisotropic plasticity models using a line search method, Computer Methods in Applied Mechanics and Engineering 317 (2017) 526–553.

[18] B. T. Lester, W. M. Scherzinger, Trust-region based return mapping algorithm for implicit integration of elastic-plastic constitutive models, International Journal for Numerical Methods in Engineering 112 (2017) 257–282. doi:10.1002/nme.5515.

[19] M. Ortiz, P. M. Pinsky, R. L. Taylor, Operator split methods for the numerical solution of the elastoplastic dynamic problem, Computer Methods in Applied Mechanics and Engineering 39 (1983) 137–157.

[20] D. Peirce, C. F. Shih, A. Needleman, A tangent modulus method for rate dependent solids, Computers & Structures 18 (5) (1984) 875–887.

[21] J. Simo, T. Hughes, Computational Inelasticity, Vol. 7 of Interdisciplinary Applied Mathematics, Springer-Verlag, New York, NY, 1998.

[22] J. Nocedal, S. J. Wright, Numerical Optimization, 2nd Edition, Springer Series in Operations Research and Financial Engineering, Springer Science+Businees Media, New York, NY, 2006.

[23] Sierra/SM Development Team, Sierra/SM 4.40 user's guide, SAND Report 2016-2707, Sandia National Laboratories, Albuquerque, NM and Livermore, CA (2016).

[24] O. C. Zienkiewicz, I. C. Cormeau, Visco-plasticity – plasticity and creep in elastic solids – a unified numerical solution approach, International Journal for Numerical Methods in Engineering 8 (1974) 821–845.

[25] I. Cormeau, Numerical stability in quasi-static elasto/visco-plasticity, International Journal for Numerical Methods in Engineering 9 (1975) 109–127.

[26] T. J. R. Hughes, R. L. Taylor, Unconditionally stable algorithms for quasi-static elasto/visco-plastic finite element analysis, Computers & Structures 8 (1978) 169–173.

[27] J. C. Simo, S. Govindjee, Non-linear B-stability and symmetry preserving return mapping algorithms for plasticity and viscoplasticity, International Journal for Numerical Methods in Engineering 31 (1991) 151–176.

Internal Distribution:

MS-0346	K. Ford	Org. 1556
MS-0523	K. Ewsuk	Org. 2631
MS-0836	M. Martinez	Org. 1516
MS-0840	J. Bishop	Org. 1554
MS-0840	E. Corona	Org. 1554
MS-0840	H. E. Fang	Org. 1554
MS-0840	B. Lester	Org. 1554
MS-0840	K. Long	Org. 1554
MS-0840	B. Reedlunn	Org. 1554
MS-0840	W. Scherzinger	Org. 1554
MS-0845	J. Thomas	Org. 1542
MS-0878	D. Kammler	Org. 2585
MS-1318	B. van Bloemen Waanders	Org. 1441
MS-1321	V. Tikare	Org. 1444
MS-1411	F. Abdeljawad	Org. 1864
MS-9042	A. Brown	Org. 8259